CPV solar cell modeling and metallization optimization

Gupta, Deepak K.; Barink, Marco; Langelaar, Matthijs

DOI
10.1016/j.solener.2017.11.015

Publication date
2018

Document Version
Final published version

Published in
Solar Energy

Solar Energy 159 (2018) 868–881

Contents lists available at ScienceDirect

Solar Energy

journal homepage: www.elsevier.com/locate/solener

CPV solar cell modeling and metallization optimization

Deepak K. Gupta[a,*], Marco Barink[b], Matthijs Langelaar[a]

[a] Precision and Microsystems Engineering, Delft University of Technology, 2628 CD Delft, The Netherlands
[b] TNO/Holst Centre, 5605 KN Eindhoven, The Netherlands

ARTICLE INFO

Keywords:
Finite element model
Topology optimization
Metallization
Concentrating solar cells
Concentrated photovoltaics
Non-uniform
Illumination
Temperature profile
Optimal design

ABSTRACT

Concentrated photovoltaics (CPV) has recently gained popularity due to its ability to deliver significantly more power at relatively lower absorber material costs. In CPVs, lenses and mirrors are used to concentrate illumination over a small solar cell, thereby increasing the incident light by several folds. This leads to non-uniform illumination and temperature distribution on the front side of the cell, which reduces performance. A way to limit this reduction is to optimize the metallization design of the solar cell for certain non-uniform illumination and temperature profiles. Most of the existing metallization optimization methods are restricted to the conventional H-pattern, which limits the achievable improvements. Topology optimization alleviates such restrictions and is capable of generating complex metallization patterns, which cannot be captured by the traditional optimization methods. In this paper, the application of topology optimization is explored for concentrated illumination conditions. A finite element model that includes all relevant resistances combined with topology optimization method is presented and the applicability is demonstrated on non-uniform illumination and temperature profiles. The finite element model allows accurate modeling of the current density and voltage distributions. Metallization designs obtained by topology optimization significantly improve the power output of concentrating solar cells.

1. Introduction

Concentrated photovoltaic (CPV) systems allow a large amount of solar power generation at a relatively lower cost, since the required solar cell material is reduced (Mellor et al., 2009). In CPV systems, lenses and curved mirrors are used to concentrate sunlight on small, but highly efficient solar cells (Baig et al., 2012). For further improvement in performance, additional elements such as sun trackers and cooling systems are also used. The use of lenses and mirrors modifies the incident radiation on the solar cells, amplifying it several folds in some parts of the cell (Baig et al., 2012). Thus, a concentrated, non-uniform illumination profile and a non-uniform temperature distribution are created on the front side of the cell. Due to illumination being higher in some parts of the cell, the photoillumination current density as well as temperature increase locally, leading to a higher voltage drop and increased ohmic losses. Mitchell (1977) showed that under non-uniform illumination, series resistance can lead to significant reductions in power output.

For a CPV system to be efficient, it is important that each of its elements performs well individually as well as collectively. One of the ways to improve the efficiency of CPVs is to improve the design of the metallization patterns of the solar cells. Optimization of metallization has been rigorously studied in the past in the context of uniform illumination and one sun intensity (Beckman, 1967; Flat and Milnes, 1979; Conti, 1981; Burgers, 1999; Gupta et al., 2014). In addition, there exist works on designing efficient metallization patterns for certain solar cell geometries under higher sun concentrations with uniform illumination (Moore, 1979; Algora and Díaz, 2000; Bissels et al., 2011). However, optimizing the metal grids under non-uniform sun intensity has received relatively little attention. Mellor et al. (2009) optimized a conventional H-pattern metallization for a Gaussian illumination profile and constant temperature, and showed that the solar cell with such metallizations could perform better under non-uniform illumination conditions. Domenech-Garret (2011) studied the effect of several illumination and temperature profiles on the performance of solar cells. In these studies, linear concentrators were considered and non-uniformity was only assumed along the finger direction (Mellor et al., 2009; Domenech-Garret, 2011). Shifts in the illumination profile due to tracking misalignment and the non-uniformity in the busbar direction were not considered. Both studies restricted themselves to H-patterns and spacing between the metal finger lines was optimized.

The H-pattern is known to be a very efficient metallization geometry for uniformly illuminated, constant temperature cells. However, for CPV, it is likely that other patterns are superior given the non-uniform

* Corresponding author.
E-mail addresses: D.K.Gupta@tudelft.nl, guptadeepak2806@gmail.com (D.K. Gupta).

https://doi.org/10.1016/j.solener.2017.11.015
Received 16 August 2017; Received in revised form 2 November 2017; Accepted 8 November 2017
Available online 29 November 2017
0038-092X/

illumination and temperature conditions. While simplifying the optimization, geometrical restrictions (*e.g.* assumption of straight metal fingers oriented parallel to each other, as in H-pattern) reduce the flexibility of the optimization process and only limited improvements in performance can be expected. More general metallization geometries have been explored for solar cells under uniform illumination as well. Burgers (1999) presented a two-step approach to optimize solar cell front metallizations without any pre-assumptions of topology. In the first step, a smeared version of electrode material distribution is optimized in the whole domain. The second step involves a heuristic procedure to translate the optimized material distribution into a line pattern. During the translation step, some prior information is needed from the side of the designer (Burgers, 2005). The applicability of this approach for non-uniform illumination was briefly discussed.

In an earlier study concerned with uniform illumination and one sun intensity (Gupta et al., 2014), we have presented a topology optimization (TO) formulation that can optimize the metallization patterns without any interference from the side of the user. TO does not impose any restriction on the design of the metal grids and is capable of generating metallization patterns that cannot be obtained with any of the previously existing methods (Gupta et al., 2015). An application where the advantage of TO has been particularly clear is the design of metallization patterns for freeform solar cells, where the traditional patterns are not suited and intuition based designs are far from optimal (Gupta et al., 2016, 2017). Under higher illumination intensity (more than one sun), the photoillumination current density is increased, which in turn leads to a larger voltage drop on the front side of the cell. Due to increased non-uniformity of the voltage profile, relatively larger power losses occur and the solar cell efficiency is reduced. This effect is more prominent under nonuniform illumination, where it is seen that the efficiency of the solar cells drops dramatically (Johnston, 1998; Luque et al., 1998; Mellor et al., 2009). Thus, it is of interest to optimize the metal grids with minimal restrictions on the design and tailor them for certain illumination and temperature profiles. With TO, it is not required to restrict the non-uniformity only in x-direction. In this study, we optimize the metallization designs for more general illumination and temperature profiles, with non-uniformity in two dimensions, using topology optimization.

During the optimization, it is important that at every iteration, the current and voltage distributions on the front side of the cell are modeled accurately. For this purpose, the finite element method (Zienkiewicz et al., 2005) is a very suited approach, and has been used in the past (Burgers, 1999, 2005; Mellor et al., 2009; Domenech-Garret, 2011; Wong et al., 2011). In Mellor et al. (2009) and Domenech-Garret (2011), COMSOL© models have been used for FEM based modeling, however, only limited mathematical details of the numerical model are discussed. A discussion of FEM based implementation is provided in Burgers (2005), where the numerical model is embedded into a two-step optimization scheme for metallization design. Further, the TO based approach presented by us in Gupta et al. (2014, 2015) uses a two-dimensional finite element scheme for modeling the local current densities and voltage distributions. However, this simplified model did not include the shunt resistance and resistance due to contact of the emitter with the metal electrode material, and is limited to uniform illumination and temperature conditions for a single sun intensity. Although the role of contact resistance can be neglected for good devices, this may not be true in general. More importantly, the allowable contact resistance is inversely proportional to the current density, due to which it becomes important for concentrated illumination conditions (Schroder and Meier, 1984).

To enable accurate modeling and optimization of concentrating solar cells, this paper presents an advanced two-dimensional finite element model and a topology optimization strategy. The numerical model can be used to accurately model the current density and voltage distributions on the front surface of the solar cell. Contact and shunt resistances are included in the model and the effect of contact resistance on the solar cell performance is studied. The numerical model is generalized for 1-diode and 2-diode models as well as other empirical I-V relations. Based on this numerical model, a topology optimization formulation and the associated adjoint sensitivity analysis are developed. The proposed topology optimization methodology can optimize the metallization patterns for solar cells under concentrating, non-uniform illumination and temperature conditions. While the focus of this paper is on CPV applications, the presented model as well as the optimization strategy are equally applicable for uniform illumination conditions. The numerical implementations are kept generic for follow up research and a MATLAB® implementation of the modeling and optimization procedure is provided.[1] Using the proposed method, metallization patterns are optimized for several cases, and relative performance improvements of up to 26% are observed.

The outline for the rest of the paper is as follows. Section 2 discusses the formulation of the two-layer finite element model. The results obtained from the numerical model for several tests are presented in Section 3. This includes numerical tests related to validation of the proposed numerical model against the results reported in Mellor et al. (2009) (Section 3.2), and study of the effect of contact resistance (Section 3.3). Section 4 presents the optimization strategy and the obtained results for various illumination and temperature profiles are presented in Section 5. Finally, the conclusions related to this work are stated in Section 6.

2. Modeling approach

In this section, a detailed numerical model is presented that can efficiently model the current flow and voltage distributions on the front surface of the solar cell. While the discussion is restricted to modeling only the front metallization pattern, the rear side can as well be modeled with slight modifications. To adapt the model for the rear side metallization design, see (Gupta et al., 2017).

2.1. Equivalent circuit

Fig. 1 shows a simple solar cell circuit diagram applicable to both the 1-diode (Shockley, 1950) as well the 2-diode model (Wolf and Rauschenbach, 1963). Based on this circuit diagram, the characteristic equation for the solar cell can then be stated as

$$I = I_L - I_{d1} - I_{d2} - I_{SH}, \tag{1}$$

where I, I_L, I_{d1}, I_{d2} and I_{SH} denote the output current, photoillumination current, the reverse saturation diode currents across diodes 1 and 2 and the shunt current, respectively. Let V_j denote the junction potential, then Eq. (1) can be rewritten as

$$I = I_L - I_{01}\left(e^{\frac{\beta V_j}{n_1}} - 1\right) - I_{02}\left(e^{\frac{\beta V_j}{n_2}} - 1\right) - \frac{V_j}{R_{SH}}. \tag{2}$$

Here, n_1 and n_2 are the ideality factors for diode 1 and 2, respectively and $\beta = \frac{q}{k_B T}$, where q, k_B and T denote elementary charge, Boltzmann's constant and absolute temperature of the cell, respectively. For a 1-diode model, n_1 and n_2 can be set to 1 and ∞ respectively and for a 2-diode model to 1 and 2, respectively. The shunt resistance R_{SH} can occur due to defects in the active layer. Due to this, a certain part of the current, termed as shunt current I_{SH} can take an alternate path (Wolf and Rauschenbach, 1963). In case there are no defects in the circuit, R_{SH} can be set to ∞, and no shunt current is generated.

Next, the junction potential V_j is further expressed as

$$V_j = V + IR_s, \tag{3}$$

where V is the voltage across the circuit and R_s denotes the total series

[1] A MATLAB® implementation is available to download from the repository at https://github.com/dkgupta90/topsol.

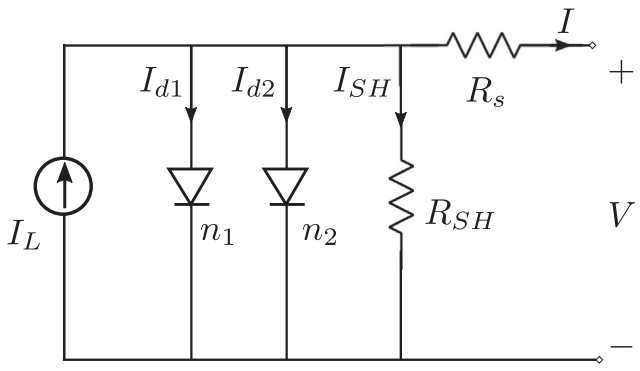

Fig. 1. Equivalent electrical circuit diagram for a solar cell.

resistance. Here, R_s can consist of contributions from emitter sheet resistance R_e, ohmic contacts to the emitter $R_{c,e}$, metal finger resistance R_{fi}, busbar resistance R_b, contributions from the wafer edges R_{edge}, resistance of the bulk material referred as base resistance R_{base}, and resistance due to the contact of the metal electrode on the rear side $R_{c,r}$. Thus, it can be stated as

$$R_s = R_e + R_{c,e} + R_{fi} + R_b + R_{edge} + R_{base} + R_{c,r}. \tag{4}$$

For the sake of simplicity, the resistive components associated with the rear side as well as the edges, *i.e.*, $R_{c,r}$ and R_{edge}, are ignored. However, the inclusion of resistive components associated with the rear side should be evident from the model description and from the study presented in Gupta et al. (2017). With these simplifications, R_s can be restated as

$$R_s = R_e + R_{c,e} + R_{fi} + R_b + R_{base}. \tag{5}$$

The electrical circuit shown in Fig. 1 is a lumped model, however, to correctly model the current and voltage distributions in the emitter and electrode layers, a distributed diode model is required (*e.g.* Galiana et al., 2005). In this paper, a distributed model is used, where the current flow at any point in the active layer is modeled using a diode and the current flow in the emitter and the electrode layers is modeled using a two-layer finite element mesh, as discussed in Section 2.3. Let the current entering the emitter layer at any point be denoted by I^e, then based on Eqs. (2) and (3),

$$I^e = I_L - I_{01}\left(e^{\frac{\beta(V+I^e\widetilde{R}_s)}{n_1}} - 1\right) - I_{02}\left(e^{\frac{\beta(V+I^e\widetilde{R}_s)}{n_2}} - 1\right) - \frac{V + I^e\widetilde{R}_s}{R_{SH}}. \tag{6}$$

Note that in Eq. (6), $\widetilde{R}_s$ only includes the base resistance and any additional resistances associated with the active layer. The resistances associated with the emitter and electrode layers (R_e,$R_{c,e}$,R_{fi} and R_b) are excluded, since they are separately modeled using the finite element mesh.

2.2. Illumination and temperature distribution

In this study, solar cells with various illumination and temperature profiles are considered. Illumination profiles for linear concentrators have been identified to be Gaussian (Johnston, 1998). While any profile can be used in our numerical model, following the work presented in Domenech-Garret (2011), we use the Gaussian radiation profiles for this study. The one-dimensional Gaussian profiles used for model validation are same as that used in Mellor et al. (2009) and Domenech-Garret (2011). However, since we do not restrict the radiation to vary only along the finger direction, two-dimensional illumination non-uniformities are modeled as well. To account for a Gaussian radiation profile, we define the radiation factor as

$$\mathscr{R}(r) = \frac{N_0 A_0}{\zeta} e^{\frac{r-r_0}{2S^2}}, \tag{7}$$

where $\mathscr{R}(r)$ denotes the radiation factor at any point $r = (x,y)$ of the solar cell front surface domain, and r_0 refers to the radiation profile center. Also, N_0 denotes the average number of suns at any point of the solar cell and S controls the width of the Gaussian curve. For the Gaussian radiation profiles used in this study, $S = \frac{4r_{max}}{\sqrt{\pi}A_0}$ and $r_{max} = \sqrt{1 + \frac{L_y}{L_x}}$, where L_y and L_x denote the cell lengths in y- and x-directions, respectively. The term A_0 controls the illumination contrast and ζ is a normalizing term defined as $\zeta = \int_\Omega e^{\frac{r-r_0}{2S^2}} d\Omega$, where Ω refers to the solar cell domain. A more complex radiation distribution is an irregular profile (caused due to misalignments, optical aberrations (Luque et al., 1998)) which is modeled by adding multiple Gaussian and anti-Gaussian profiles.

Under non-uniform temperature distribution, the terms I_{01} and I_{02} in Eq. (6) are no longer constant in the whole solar cell domain. The reverse saturation diode currents can be expressed as functions of local temperature as Mellor et al. (2009),

$$I_{01} = I_{001} T^3 e^{\frac{-E_{G0}}{k_B T}}, \tag{8}$$

$$I_{02} = I_{002} T^3 e^{\frac{-E_{G0}}{k_B T}}, \tag{9}$$

where I_{001},I_{002} and E_{G0} (bandgap energy at 0 K) can be assumed to be constant with respect to temperature.

The temperature profile depends on several factors, *e.g.* the distribution of incident illumination, solar cell properties, cooling device, *etc.*, and simulating it for a certain specific scenario is beyond the scope of this paper. The choice of the temperature profile does not affect the proposed modeling and optimization approach, hence we restrict ourselves to some of the popularly used temperature profiles. In Domenech-Garret (2011), it is stated that two of the prominent temperature profiles for concentrators are the Gaussian and anti-Gaussian distributions. For Gaussian radiation profiles, temperature field in silicon solar cells can be described using Gaussian distributions (Franklin and Coventry, 2003). Temperature profiles can also be considered such that they describe the role of cooling devices. Under such scenarios, the temperature distribution can be described using an inverse Gaussian distribution (Domenech-Garret, 2011). Similar to radiation profiles, we do not restrict the temperature to vary only along the finger direction, rather two-dimensional temperature non-uniformities are modeled as well.

The Gaussian temperature distribution can be described as

$$T_g(r) = \Delta T e^{\frac{-(r-r_0)^2}{2S_T^2}} + T_0, \tag{10}$$

where ΔT denotes the amplitude of temperature with respect to the baseline temperature T_0 and S_T controls of the width of the temperature curve. The anti-Gaussian profile can be described as

$$T_{ag}(r) = \Delta T\left(1 - e^{\frac{-(r-r_0)^2}{2S_T^2}}\right) + T_0. \tag{11}$$

2.3. Finite element model

We model the solar cell using the finite element method (FEM). Fig. 2 shows a two-layer finite element model for the front surface of a solar cell. The lower layer models the voltage and current distributions for the emitter layer and the upper layer similarly models these parameters for the metal electrode. The metallization pattern is defined on the upper layer, and this pattern is optimized using a density-based topology optimization approach (Bendsøe and Sigmund, 2003). For optimization purposes, the metallization is defined using a set of density design variables $\boldsymbol{\rho}$ comprising the element densities for each finite element. The term *density* here quantifies the amount of electrode material inside each finite element of the metallization layer. For a density

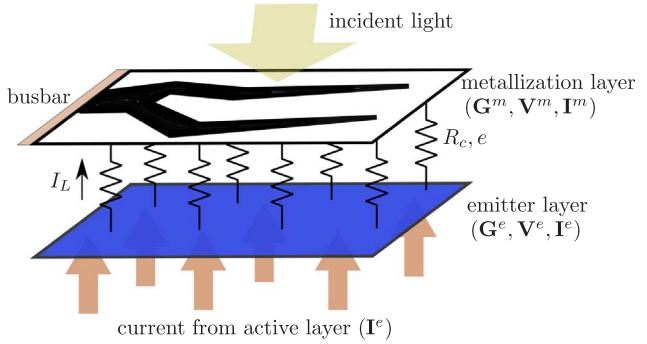

Fig. 2. A two-layer finite element model of the front surface of a solar cell. Layer 1 comprises the emitter material and layer 2 consists of electrode material parts and void parts. Each node of the emitter layer is connected to the respective node in the metal layer with a resistor (contact resistance $R_{c,e}$).

value of 1, the finite element is fully filled with electrode material and for 0, it is empty.

The reason to use a two-layer model is to accurately model the contact resistance $R_{c,e}$ between the electrode material and the emitter. In general, losses due to the ohmic contact (contact resistance) depend on the current flow between the metal and the emitter layer. Thus, rather than the whole area of metal-emitter contact, only those parts need to be considered where there is a current flow between the two layers. In the proposed numerical model, this is achieved with two layers of finite element mesh, where every node of the emitter layer is connected to the corresponding node of the metal layer with a resistor of resistance $R_{c,e}$. The losses due to local ohmic contact can then take place only if there is a flow of current through the respective resistor $R_{c,e}$.

To model the current and voltage distributions, the following partial differential equations need to be solved:

$$\sigma^e \nabla^2 V^e = \frac{\delta \widetilde{\rho}^e}{\delta t}, \tag{12}$$

$$\sigma^m \nabla^2 V^m = \frac{\delta \widetilde{\rho}^m}{\delta t}. \tag{13}$$

Here and henceforth, the superscripts e and m refer to the emitter and metal electrode layers, respectively. The material dependent conductivities are represented by σ and $\widetilde{\rho}$ refers to enclosed charge density. Based on finite element discretizations (*e.g.* Zienkiewicz et al., 2005), the systems of equations for the two layers are

$$\mathbf{G}^e\mathbf{V}^e - \mathbf{I}^e(\boldsymbol{\rho}, \mathbf{V}^e) + \mathbf{I}^m(\mathbf{V}^e, \mathbf{V}^m) = \mathbf{0}, \tag{14}$$

$$\mathbf{G}^m(\boldsymbol{\rho})\mathbf{V}^m - \mathbf{I}^m(\mathbf{V}^e, \mathbf{V}^m) = \mathbf{0}. \tag{15}$$

The conductivity matrices are denoted by $\mathbf{G}$, and $\mathbf{V}$ and $\mathbf{I}$ refer to the column vectors of voltage and current, respectively.

The current $\mathbf{I}^e$, coming from active layer and entering the emitter layer, depends on the local shading. Here, local shading refers to the amount of sunlight blocked by the electrode metal in a certain part of the cell, and is dependent on the element density of the respective finite element in the metallization layer. On the other hand, $\mathbf{I}^m$, the ohmic current flowing from the emitter layer to the metal electrode, does not depend on the electrode material distribution. This current depends on the contact resistance $R_{c,e}$ and can be expressed as

$$\mathbf{I}^m = \frac{1}{R_{c,e}}(\mathbf{V}^e - \mathbf{V}^m). \tag{16}$$

Using Eqs. (14)–(16), the system of equations can be combined into a residual form as

$$\mathbf{R} = \begin{bmatrix} \mathbf{G}^e & \mathbf{0} \\ \mathbf{0} & \mathbf{G}^m \end{bmatrix} \begin{bmatrix} \mathbf{V}^e \\ \mathbf{V}^m \end{bmatrix} - \begin{bmatrix} \mathbf{I}^e \\ \mathbf{0} \end{bmatrix} + \frac{1}{R_c} \begin{bmatrix} \mathbb{I} & -\mathbb{I} \\ -\mathbb{I} & \mathbb{I} \end{bmatrix} \begin{bmatrix} \mathbf{V}^e \\ \mathbf{V}^m \end{bmatrix} = \mathbf{0}. \tag{17}$$

Eq. (17) can further be written as

$$\mathbf{R} = \underbrace{\begin{bmatrix} \mathbf{G}^e + \frac{1}{R_c}\mathbb{I} & -\frac{1}{R_c}\mathbb{I} \\ -\frac{1}{R_c}\mathbb{I} & \mathbf{G}^m + \frac{1}{R_c}\mathbb{I} \end{bmatrix}}_{\mathbf{G}} \underbrace{\begin{bmatrix} \mathbf{V}^e \\ \mathbf{V}^m \end{bmatrix}}_{\mathbf{V}} - \underbrace{\begin{bmatrix} \mathbf{I}^e \\ \mathbf{0} \end{bmatrix}}_{\mathbf{I}} = \mathbf{G}\ \mathbf{V} - \mathbf{I} = \mathbf{0}. \tag{18}$$

The conductivity matrix $\mathbf{G}^e$ is constructed from the global assembly of the element conductivity matrices $\mathbf{G}^e_{el}$, where

$$\mathbf{G}^e_{el} = \sigma^e_s \mathbf{G}_0. \tag{19}$$

Here, σ^e_s denotes the sheet conductivity of the emitter material and $\mathbf{G}_0$ denotes the normalized conductivity matrix (Gupta et al., 2015). The conductivity for layer 2 depends on the electrode material distribution and can be described using the Solid Isotropic Material with Penalization (SIMP) model (Bendsøe, 1989) as follows:

$$\mathbf{G}^m_{el} = \sigma^0_s + \rho^p(\sigma^m_s - \sigma^0_s)\mathbf{G}_0, \tag{20}$$

where σ^m_s denotes the sheet conductivity of the constant thickness electrode material and σ^0_s is chosen as $10^{-12}\cdot\sigma^m_s$ to represent physically void areas. A non-zero value is chosen to avoid numerical instabilities. To include the shading effect of the metallization into the model, I_L in Eq. (6) is replaced by $I_L(1-\rho)^r$. Both p and r exponents are used to penalize intermediate element densities. This is necessary from a fabrication point of view, since it helps to obtain 0 (electrode material) or 1 (void) values in the final metal layer.

The busbar is assumed to be directly connected to the external load and is therefore set to the cell operating voltage V_b. For optimal performance of the solar cell, the busbar potential is also considered as an optimization parameter. Next, the nonlinear system of equations (Eq. (17)) is solved in an iterative manner using the Newton method. An initial guess for $\mathbf{V}$ is made and at every iteration, it is updated as follows:

$$\mathbf{V}_{i+1} = \mathbf{V}_i - \left(\frac{d\mathbf{R}_i}{d\mathbf{V}_i}\right)^{-1} \mathbf{R}_i, \tag{21}$$

where

$$\frac{d\mathbf{R}_i}{d\mathbf{V}_i} = \mathbf{G} - \frac{d\mathbf{I}_i}{d\mathbf{V}_i}, \tag{22}$$

$$\frac{d\mathbf{I}_i}{d\mathbf{V}_i} = \begin{bmatrix} \frac{d\mathbf{I}^e_i}{d\mathbf{V}^e_i} & \mathbf{0} \\ \mathbf{0} & \mathbf{0} \end{bmatrix}. \tag{23}$$

During optimization, the Newton iterations can be started from the solution of $\mathbf{V}$ obtained in the previous optimization step. At every Newton iteration, $\mathbf{I}^e$ and $\frac{d\mathbf{I}^e}{d\mathbf{V}^e}$ need to be calculated, details of which are given in Appendices A and B, respectively.

3. Modeling results

To validate the proposed numerical model, the numerical solar cell example presented in Mellor et al. (2009) is modeled and the results are compared. Further, based on our numerical model, the effect of contact resistance on the performance of solar cell is studied for uniform and non-uniform illumination conditions. For model validation as well as for optimization, numerical examples of crystalline silicon solar cell are used in this paper. However, the proposed approach is general and also applicable to other solar cell types. In the past, variants of the method have been used for other cell types such as thin films (Gupta et al., 2014), organic cells (Gupta et al., 2017).

3.1. Model parameters

A monocrystalline silicon solar cell of dimensions 4.8 cm × 10.6 cm is considered with a busbar width of 2 mm and finger width of 35 μm. Additional input parameters used in our numerical model are the same

Table 1
Input parameters for a solar cell under 12 suns illumination (from Mellor et al. (2009)).

Cell geometry and resistivities	
Cell length (L_y)	10.6 cm
Cell width (L_x)	4.8 cm
Busbar width	2 mm
Finger width	35 μm
Finger sheet resistance	1.05×10^{-3} Ω/sq
Emitter sheet resistance	100 Ω/sq
Operation conditions	
Temperature	320 K
Mean illumination intensity	12,000 W m^{-2}
Diode parameters	
C_1	0.39444 A W^{-1}
C_2	−11,739 A m^{-2} K^{-3}
C_3	−0.83584 A m^{-2} V^{-1}
Ideality factor n_1	1.0603
E_g	1.124 eV

as that in Mellor et al. (2009) and are stated in Table 1. Note that in Rosell and Ibañez (2006) and Mellor et al. (2009) as well as several other works related to concentrated illuminations, a different current–voltage characteristic relationship is used. Here, current density and voltage are related as follows:

$$J^e = C_1 G + C_2 T^3 \left(e^{\frac{-E_g}{k_b T}}\right)\left(e^{\frac{qV}{n_1 k_b T}} - 1\right) + C_3 V, \tag{24}$$

where J^e and G denote current density in the emitter layer and illumination, respectively, and C_1,C_2 and C_3 are coefficients specific to any given cell (Rosell and Ibañez, 2006). The parameters C_1,C_2 and C_3 listed in Table 1 are related to this curve. However, for modeling purpose, this is not a problem and it can be transformed into the traditional IV curve listed in Eq. (6) (see Appendix C).

For traditional solar cells, where an H-pattern is used for metallization, the size of the modeling domain can be significantly reduced due to the lines of symmetry along the *x*- and *y*-directions. Thus, we model here only one cell element as shown in Fig. 3. For FEM based modeling, the domain of the element is discretized into a structured grid of square elements with bilinear shape functions. The operating voltage of the cell is optimized to achieve maximum performance for the chosen metallization design.

3.2. Model validations

For validation purposes, two different illumination conditions are considered. For the first test, a uniform illumination of 12 suns is assumed on the front side of the solar cell. The optimal metallization design for this scenario consists of 184 parallel metal fingers (Mellor et al., 2009). The cell element domain is modeled using 4400×117 square finite elements. Fig. 4 shows the illumination profile as well as the current and voltage distributions modeled on the front side of one cell element. The fill factor (FF) and efficiency η values obtained using the proposed model are 0.79 and 19.25%. These values match with those obtained in Mellor et al. (2009), where FF and η are equal to 0.79 and 19.25%, respectively.

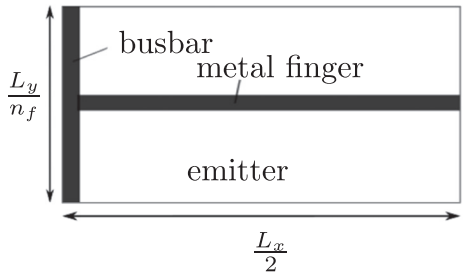

Fig. 3. The cell element used for modeling purposes. Here, L_x and L_y are the cell lengths along x- and y-directions and n_f denotes the number of metal fingers.

In another test, a Gaussian illumination profile with a mean illumination of 12 suns and peak to mean ratio (PIR) of 10 is used. The metallization geometry is assumed to still consist of 184 fingers, which is an optimal geometry of electrode fingers under uniform illumination. With this metallization, the FF and η values drop to 0.73 and 17.49%, respectively. For the non-uniform illumination of PIR = 10, the optimized metallization geometry consists of 287 electrode fingers (Mellor et al., 2009). For this case, the cell element is modeled using 4400×84 electrode fingers. With this metallization, it is observed that the efficiency improves from 17.49% to 18.58% and FF increases from 0.73 to 0.80. The Fig. 5 shows the illumination profile, voltage and current distributions for one cell element.

For uniform as well as non-uniform illumination, it is observed that the FF as well as η values obtained using the proposed numerical model match well with the results in Mellor et al. (2009). Table 2 also reports additional parameters associated with the output IV curves. These values also match well with those stated in Mellor et al. (2009). Thus, it is observed that the proposed model can accurately model the published solar cell cases of uniform and non-uniform illumination conditions.

3.3. Effect of contact resistance

Compared to the effect of other series resistances, generally the effect of contact resistance is very small and can generally be neglected. However, as stated in Schroder and Meier (1984), Meier and Schroder (1984), and van Deelen et al. (2016), this holds for good devices and may not be true in general. The effect of contact resistance is more prominent under concentrated conditions. Thus, in the proposed finite element model, the ohmic contact between the emitter layer and the metal electrode is also modeled. Based on the model, here we briefly study the effect of contact resistivity $\rho_{c,e}$ on the performance of a solar cell. Here, contact resistivity is chosen in place of contact resistance, since it is an area independent parameter. To study its effect, the solar cell example of Mellor et al. (2009) is studied and the input parameters stated in Table 1 are used.

Fig. 6 shows efficiency for several values of contact resistivity $\rho_{c,e}$ for a uniform as well as a non-uniform illumination profile under an intensity of 12 suns. For uniform illumination, it is observed that for a $\rho_{c,e}$ value close to 10^{-8} Ω m^2, the drop in efficiency is less than 0.04%, which is negligible. This result is in line with (Schroder and Meier, 1984), where it has been stated that such a value of $\rho_{c,e}$ should be adequate. However, it is important to note that if the contact resistivity is high, the performance of the cell is significantly affected. For example, for $\rho_{c,e}$ equal to 10^{-7} Ω m^2, the efficiency drops by 0.23% and for 10^{-6} Ω m^2, an efficiency drop of more than 2% is observed. Clearly, it shows that the contact resistance, if large, can significantly reduce the power output from a solar cell.

Under non-uniform illumination, the role of contact resistance is even more prominent. For a $\rho_{c,e}$ value of 10^{-9} Ω m^2, the drop in efficiency is close to 0.04%. However, unlike uniform illumination, the efficiency is reduced by more than 0.2% for $\rho_{c,e}$ equal to 10^{-8} Ω m^2. Thus, under a non-uniform illumination profile, the drop in performance is larger. For $\rho_{c,e}$ equal to 10^{-7} Ω m^2, an efficiency drop of around 1.5% is observed. Thus, based on these numerical experiments, it can be seen that contact resistance can play an important role in determining the performance of a concentrating solar cell.

4. Optimization approach

4.1. Optimization problem

The solar cell power maximization problem is an unconstrained

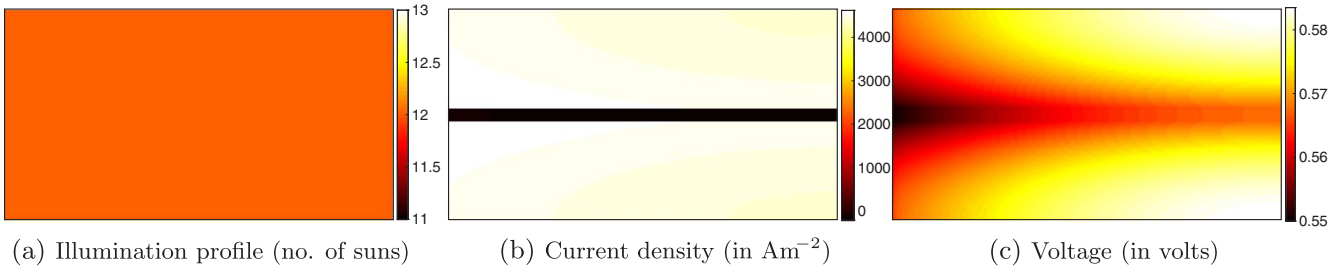

Fig. 4. Uniform illumination profile for 12 suns and the out-of-plane current density and voltage distributions observed in one cell element (1 sun = 1000 W m^{-2}).

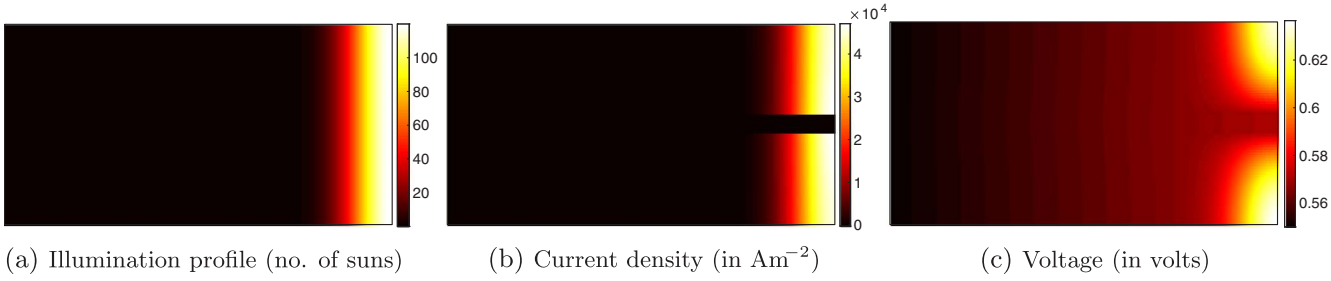

Fig. 5. Non-uniform illumination profile with an average illumination of 12 suns and peak illumination ratio of 10 and the out-of-plane current density and voltage distributions observed in one cell element (1 sun = 1000 W m^{-2}).

Table 2
Number of electrode fingers used and respective output IV characteristics obtained using our model and those reported by Mellor and co-workers.

Parameter	Our results	Mellor et al. (2009)
Uniform illumination with 12 suns (using 184 metal fingers)		
I_{sc} (in A)	20.69	20.79
V_{oc} (in volts)	0.66	0.65
Fill factor	0.79	0.79
Efficiency (in %)	19.25	19.25
Average illumination of 12 suns with PIR = 10 (using 184 metal fingers)		
I_{sc} (in A)	20.69	–
V_{oc} (in volts)	0.65	0.64
Fill factor	0.73	0.73
Efficiency (in %)	17.49	17.50
Average illumination of 12 suns with PIR = 10 (using 287 metal fingers)		
I_{sc} (in A)	20.02	–
V_{oc} (in volts)	0.65	0.65
Fill factor	0.80	0.80
Efficiency (in %)	18.58	18.60

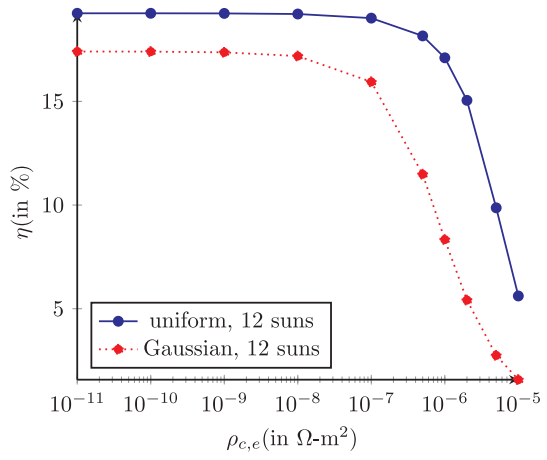

Fig. 6. Effect of resistivity of the ohmic contact between the emitter and electrode, $\rho_{c,e}$, on the efficiency of a solar cell.

optimization problem. To formulate the objective function, Kirchoff's law is used according to which all the generated current in the domain must pass through the busbar which is set to a potential V_b. Thus, the power output P_{out} for the solar cell is expressed as

$$P_{out} = V_b \sum_{i=1}^{N_{el}} I_i^m = V_b \sum_{i=1}^{N_{el}} I_i^e, \tag{25}$$

where I_i^e and I_i^m denote the currents in the ith finite element of the emitter and electrode metal layers, respectively, and N_{el} denotes the number of finite elements in either of the layers.

Traditionally, most of the optimization algorithms require the problem to be posed as a minimization problem. Thus, the objective function $\mathscr{J}(\boldsymbol{\rho})$ is

$$\min_{\mathscr{J}(\boldsymbol{\rho})} \mathscr{J}(\boldsymbol{\rho}), \quad \text{with } \mathscr{J}(\boldsymbol{\rho}) = -P_{out}. \tag{26}$$

In this study, gradient-based optimization is applied, using the method of moving asymptotes (Svanberg, 1987). In general, it is observed that smaller electrode lines help to improve the solar cell performance. The optimization process would prefer to design very fine electrode features, however, from a fabrication point of view, there is a lower limit on the feature sizes. To take this into account, the optimization process needs to be constrained to not design electrode features smaller than certain minimum size. To impose a restriction on minimum feature size and to avoid any numerical artefacts, we use a density filter (Bruns and Tortorelli, 2001; Gupta et al., 2015). Filtering averages the element densities in a weighted sense within a radius r_{min}, thereby not allowing electrode features smaller than r_{min} to occur. In addition, filtering reduces the contrast in density values between the adjacent neighbors, which in turn avoids the formation of checkerboard patterns and other numerical artefacts. For details on density filtering and other alternatives, see Sigmund (2007).

Since the density values are allowed to vary from 0 to 1, it is possible that the converged solution consists of intermediate density values which are not desired from a fabrication point of view. Due to filtering, this effect is more prominent and intermediate density values are seen at the boundaries of the electrode designs. To achieve more crisp

solutions, a continuous approximation to the Heaviside function is embedded in the optimization process. The slope of the Heaviside approximation is controlled using a parameter β_H, which is initially chosen to be 1 and its value is doubled at every 50 iterations up to a maximum of 1024. For very high values of β_H, the approximation matches the exact Heaviside function very well. Such a continuation scheme has proven to converge to well performing solutions for several TO problems. The details related to the implementation of continuous Heaviside approximation can be found in Guest et al. (2004) and Sigmund (2007).

4.2. Sensitivity analysis

At every step of the optimization, gradient-based optimization algorithms require information regarding the sensitivity of the objective to each of the design variables. To compute the sensitivities, the adjoint method is used (van Keulen et al., 2005). The adjoint sensitivity analysis of $\mathscr{J}$ requires an adjoint formulation where the augmented response $\widehat{\mathscr{J}}$ is stated as

$$\widehat{\mathscr{J}}(\mathbf{s}) = \mathscr{J}(\mathbf{s},\mathbf{V}(\mathbf{s})) + \boldsymbol{\lambda}^{\mathrm{T}}(\mathbf{R}(\mathbf{s},\mathbf{V}(\mathbf{s}))), \tag{27}$$

where $\mathbf{s}$ is the set of design variables and can be expressed as $\mathbf{s} = [\rho_1,\rho_2,...,V_b]$. Using Eq. (18) and choosing $\boldsymbol{\lambda}^{\mathrm{T}} = [\boldsymbol{\lambda}_e^{\mathrm{T}} \quad \boldsymbol{\lambda}_m^{\mathrm{T}}]$, we obtain

$$\widehat{\mathscr{J}} = \mathscr{J} + \begin{bmatrix} \boldsymbol{\lambda}_e \\ \boldsymbol{\lambda}_m \end{bmatrix}^{\mathrm{T}} \left(\begin{bmatrix} \mathbf{K}^e + \frac{1}{R_c}\mathbf{I} & -\frac{1}{R_c}\mathbf{I} \\ -\frac{1}{R_c}\mathbf{I} & \mathbf{K}^m + \frac{1}{R_c}\mathbf{I} \end{bmatrix} \begin{bmatrix} \mathbf{V}^e \\ \mathbf{V}^m \end{bmatrix} - \begin{bmatrix} \mathbf{I}^e \\ \mathbf{0} \end{bmatrix} \right). \tag{28}$$

The sensitivities $\frac{d\widehat{\mathscr{J}}}{d\boldsymbol{\rho}}$ and $\frac{d\widehat{\mathscr{J}}}{dV_b}$ are obtained by taking the derivative of Eq. (28) with respect to $\mathbf{s}$, details of which are discussed in Appendix D. The total computational cost of the sensitivity analysis for all design variables corresponds to the solution time of a single Newton iteration of the nonlinear solar cell analysis. This efficient approach enables the optimization of detailed metallization topologies.

5. Optimization results

To demonstrate the applicability of the proposed methodology, a number of test cases are considered. Unlike the traditional H-pattern, where due to regularity of the metallization geometry, one cell element (as shown in Fig. 3) can be used for optimization, no such regularity is known beforehand for a TO problem. Although it is possible to perform TO on a domain size of one cell element, this would considerably restrict the design freedom of the optimization problem, and limit the performance improvement. For increased flexibility of the optimization problem, considering a larger design domain is preferable. Thus, rather than choosing just one cell element, half of the entire solar cell is used to optimize the metallization design. The input parameters used are same as those stated in Table 1. Since typically smaller solar cells are used in CPVs, the physical size of the chosen cell is 2.42 cm × 1.18 cm, and the minimum electrode width is restricted to 60 μm. The contact resistivity $\rho_{c,e}$ is set to $10^{-9}\ \Omega\ \mathrm{m}^2$.

In general, for simple illumination profiles as in Mellor et al. (2009), well performing H-pattern designs can be easily obtained. We observed that for such illuminations, it is difficult to obtain better performing designs using TO. However, for more complex illumination and temperature profiles, the gain in performance is quite significant using TO, due to which several such non-uniform illumination and temperature profiles are considered here. Three Gaussian profiles (Fig. 7a) with A_0 values of 10, 15 and 20, and an irregular profile comprising two Gaussian distributions of A_0 values 15 and 20 (Fig. 7b) are considered for defining the illumination field. The average illumination intensity for all the cases is equal to that of 12 suns. Note that these are synthetic profiles for the purpose of illustrating the optimization process. The three temperature profiles used in this work are a uniform field, a Gaussian distribution (Fig. 8a) and an anti-Gaussian (Fig. 8b) distribution. For all the three temperature profiles, the base temperature was set to 320 K and the temperature amplitude for the non-uniform profiles was set to 40 K.

The design domain of the cell is discretized using a structured mesh of 600 × 585 finite elements, and the filter radius r_{min} is set to 1.5 elements. This results in a minimum feature size of 60 μm. The mesh resolution is chosen such that the desired feature size can be accurately represented. In Gupta et al. (2015), it has been shown that the optimized designs are not dependent on the choice of mesh, and show only limited variations with change in mesh resolution. A penalty continuation scheme is used, where the exponents p and r are both set to 3 initially, and after every 50 iterations of TO, an increment of 0.5 is made to each of them. For a solar cell problem, generally the amount of electrode material to be used is decided by the optimizer based on the compromise between shading and resistive losses (Gupta et al., 2015). However, in this paper, numerical cases are considered where the illumination intensity in some regions of the cell is close to zero. In those parts, the optimizer prefers to use electrode material for a marginal gain in conductivity, which can lead to significant parts of the domain being covered with electrode material. To avoid this uneconomic use of material, a constraint is imposed that not more than 10% of the solar cell front surface can be covered with the metallization pattern.

To compare the performance of the designs obtained from TO, a reference H-pattern is used. Parallel electrode fingers of width 60 μm are used and the spacing between the fingers is optimized for a uniform illumination intensity of 12 suns and a uniform temperature distribution of 320 K. The efficiency of the reference design under various illumination and temperature conditions is denoted by η^* and the efficiency of the optimized design obtained from TO under similar conditions is denoted by η.

5.1. Illumination profiles

Figs. 9–11 show the optimized designs and the corresponding current density and voltage distributions for the front side of the solar cell for Gaussian illumination profiles with A_0 equal to 10, 15 and 20, respectively. To reiterate here, A_0 controls the illumination contrast such that for higher values of A_0, the contrast is higher and the illumination is localized in a smaller region. A uniform temperature distribution with base temperature $T_0 = 320$ K is chosen. For $A_0 = 15$ and 20, an intermediate post processing is involved where undesired electrode material from non-illuminated regions of the domain is removed, however, this does not affect the performance of the design. Fig. 12 shows the optimized designs before and after processing for $A_0 = 20$. During optimization, removing material from the almost non-illuminated parts of the cell does not help in improving its performance. Hence, some ineffective electrode material is left in dark areas in the optimized design, as can be seen in Fig. 12a. Table 3 states the solar cell efficiencies obtained using the reference design as well as TO based designs for various illumination and temperature profiles considered in this study. A general observation is that higher values of A_0 result in lower performances of the reference design (denoted by η^*) as well as the optimized design obtained from TO (denoted by η).

Among the three Gaussian profiles used, it is observed that for $A_0 = 15$ and 20, the efficiency of the solar cells increases by 1.76% and 3.48%, respectively, for the TO based design compared to the reference design. These imply relative performance improvements of approximately 11% and 26%, respectively for the two cases. However, for $A_0 = 10$, the TO based design is slightly inferior to the reference design with a reduction of around 0.38% in efficiency. We believe, it could be a locally optimal solution and with different set of parameters and starting design, it should be possible to obtain a better performing design. In general, given the freedom of design, TO based metallization should be expected to perform better. The solar cell metallization design problem is a highly non-convex problem with many locally optimal solutions in the design domain. At the same time, due to the large

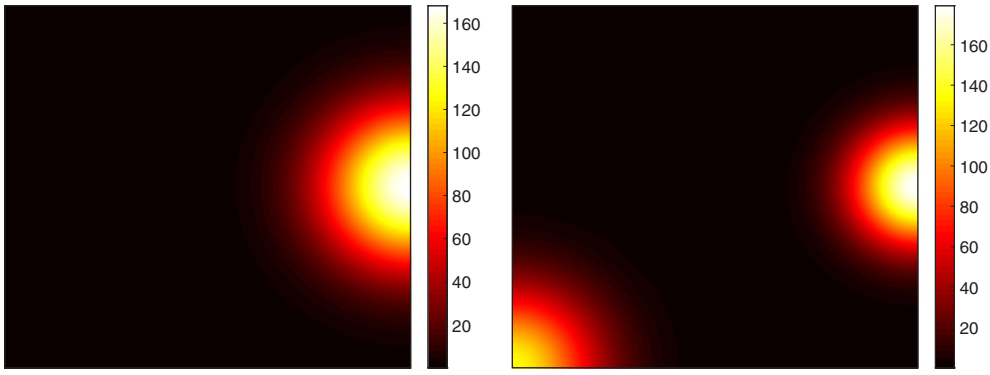

(a) Gaussian profile (b) Irregular profile

Fig. 7. Non-uniform illumination profiles with an average illumination of 12 suns (1 sun = 1000 W m^{-2}). For the Gaussian profile, A_0 is equal to 15 and for the irregular profile A_0 values are 15 and 20 for the two Gaussian distributions.

number of design variables (*e.g.* 0.3 million here), gradient-based optimization methods are used, which can occasionally converge to an inferior locally optimal solution. For the chosen illumination profiles, symmetric metallization designs are expected. However, we use the Newton method to solve Eq. (18), and due to even small numerical tolerances at any step of the optimization, the symmetry of the structure can break. For this reason, optimized designs for the solar cell obtained using TO can exhibit asymmetric features.

For the choice of $A_0 = 15$ and 20 as well as for various other cases considered in this study, it is observed that there is a voltage drop in the direction away from the busbar (*e.g.* Figs. 10c and 11c). The reason is that there are some regions in the cell domain where the illumination intensity is close to zero. Due to this, there is no illumination current generated in those areas, which leads to a net current flow in the reverse direction creating local sinks in the cell domain and drop in voltage towards these regions. However, the magnitude of this current is very small compared to the high illumination regions of the cell, and there is no significant impact on the performance of the cell due to the local current absorptions.

Next, an irregular illumination profile is used and the performance of the solar cell is evaluated. The irregular profile is formed by two Gaussian distributions ($A_0 = 15$ and 20), with the centres located in two different parts of the design domain as shown in Fig. 8b. Fig. 13 shows the optimized design and the current density and voltage distributions for the front side of the cell obtained using TO. Compared to the reference design ($\eta^* = 16.035\%$), an increase of 1.43% is observed in the solar cell efficiency when the TO based design is used ($\eta = 17.463\%$).

For all the four illumination profiles considered here, it is observed that fine features are created in regions with very high illumination intensity. This is because addition of electrode material leads to shading, and in the regions of high illumination intensity, even the addition of a small amount of electrode material leads to large reductions in the illumination, which can significantly affect the performance of the solar cell. We observed that if the restriction on the minimum electrode width is relieved, TO leads to finer electrode features and further improvement in the performance of the solar cell.

5.2. Temperature profiles

The non-uniformity in temperature distribution can also affect the performance of a solar cell. For CPVs, the concentration of sunlight in a small part of the cell leads to a non-uniform temperature profile. Additionally, the cooling systems can also create a non-uniform distribution of temperature. In this paper, we do not simulate the exact temperature profile for a certain radiation profile and cell properties, as this also requires accurate modeling of all surrounding systems and their thermal properties, which is beyond the scope of this study. Rather, the temperature profile is prescribed (as shown in Fig. 8) and the metallization design is optimized, to study its influence on the optimal design. The resulting metallizations and the current density and

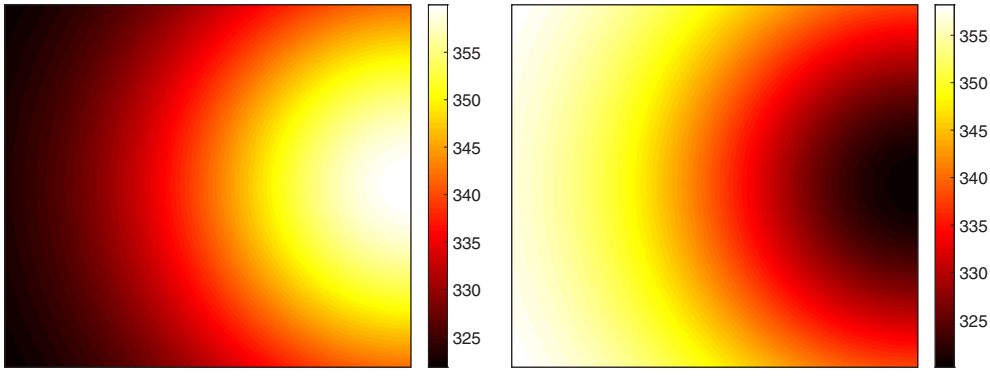

(a) Gaussian profile (b) Anti-Gaussian profile

Fig. 8. Non-uniform temperature profiles with base temperatures equal to 320 K. The temperature amplitude for both cases is set to 40 K deviation from the base temperature.

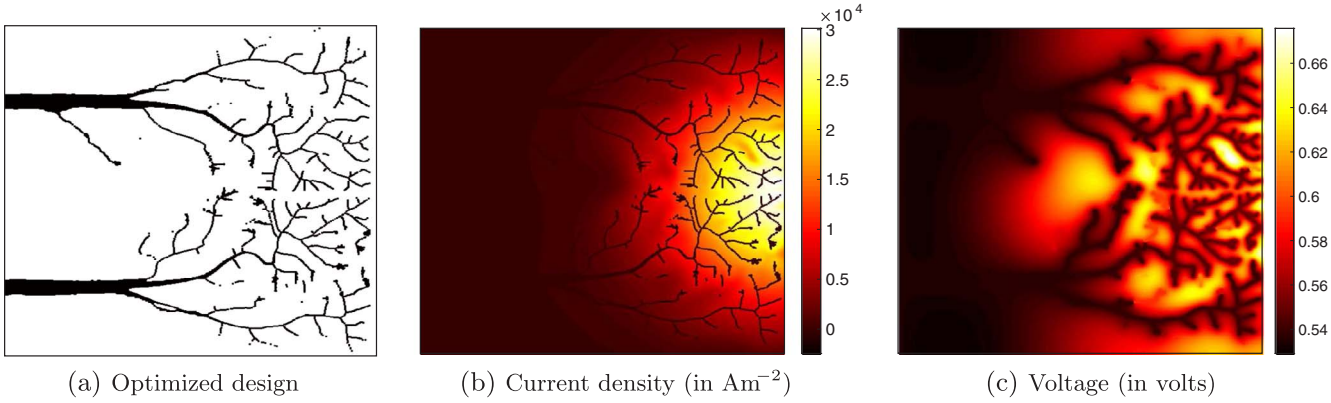

Fig. 9. Optimized design and the current density and voltage distributions for the front side of a solar cell under a Gaussian illumination of an average intensity of 12 suns ($A_0 = 10$). A uniform temperature profile is chosen with base temperature set to 320 K. The optimal busbar potential V_b and efficiency η values are 0.535 volts and 17.075%, respectively.

voltage distributions obtained using TO for the Gaussian and anti-Gaussian temperature distributions are shown in Figs. 14 and 15, respectively. The efficiency values obtained using these temperature profiles for the reference design as well as for the designs obtained using TO are stated in Table 3.

For the reference design itself, it is observed that performance of the solar cell under a non-uniform illumination profile is lower than that of the uniform distribution. The reason is that the local temperature in some parts of the cell for the non-uniform profiles is higher than the base temperature. Due to increased temperatures, the dark currents are higher in those parts, which leads to an overall reduction in the generated current density and a reduction in performance.

With TO, the performance of the solar cell is improved for both non-uniform temperature profiles (Table 3). Compared to the efficiency values of 13.425% and 14.997% obtained for the reference design for the Gaussian and anti-Gaussian temperature profiles, respectively, those obtained using TO are 15.403% and 16.271%, respectively. It is observed that the metallization designs obtained for the two cases are different from that of a uniform temperature distribution (Fig. 10). The change in temperature affects the current density and voltage distributions, which in turn affects the electrode material distribution on the front surface. Thus, for the non-uniform temperature distributions, a tailored metallization helps to improve the performance. Similar to the previous cases, small negative currents are observed in some parts of the cell, leading to absorption and a drop in voltage away from the busbar.

6. Conclusions

In this paper, a finite element method based numerical model and a topology optimization strategy have been presented to optimize solar cell metallization patterns under concentrated illumination conditions. All the relevant resistances including the contact and shunt resistance are included in the model. The proposed model is validated through comparisons with previously published modeling results for uniform and non-uniform illumination conditions. Further, from our analysis of solar cells under concentrated conditions, it is observed that contact resistance can significantly affect the performance. Compared to uniform illumination, this effect is more prominent under concentrated conditions. For example, for the case considered in this paper, it is observed that for the same value of contact resistance, the reduction in solar cell performance under concentrated illumination could be seven times more than that observed under uniform sunlight of equal average illumination. Clearly, this shows that contact resistance can be

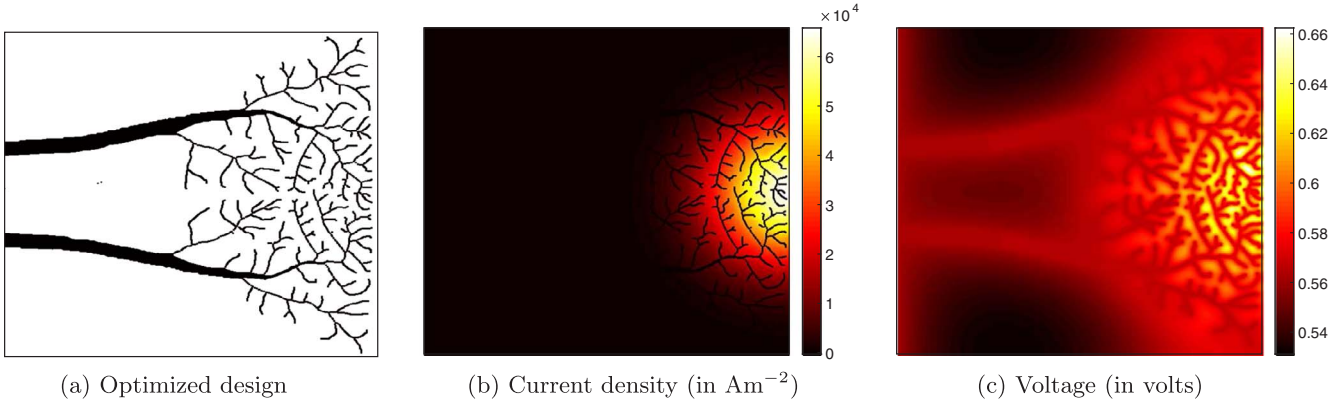

Fig. 10. Optimized design and the current density and voltage distributions for the front side of a solar cell under a Gaussian illumination of an average intensity of 12 suns ($A_0 = 15$). A uniform temperature profile is chosen with base temperature set to 320 K. The optimal busbar potential V_b and efficiency η values are 0.562 volts and 17.271%, respectively.

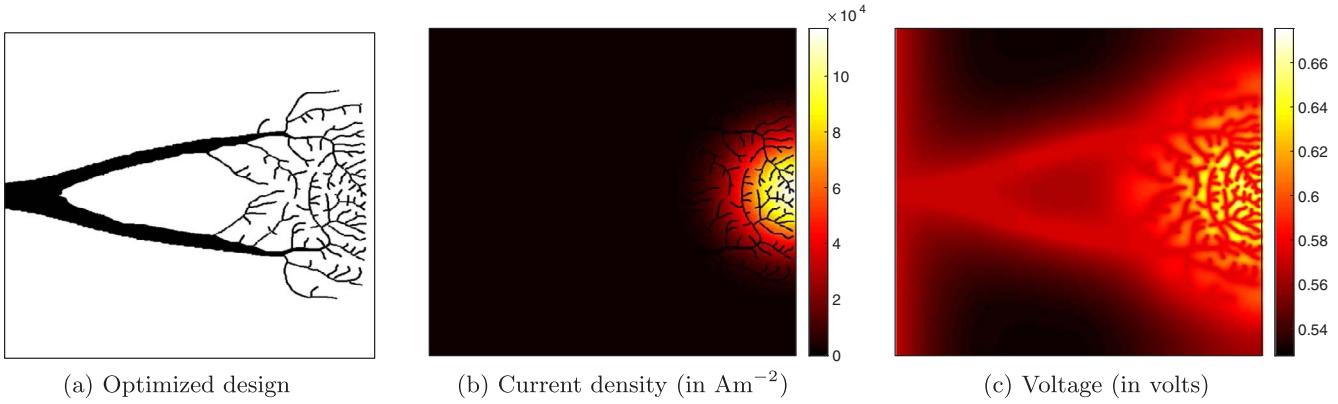

Fig. 11. Optimized design and the current density and voltage distributions for the front side of a solar cell under a Gaussian illumination of an average intensity of 12 suns ($A_0 = 20$). A uniform temperature profile is chosen with base temperature set to 320 K. The optimal busbar potential V_b and efficiency η values are 0.566 volts and 16.846%, respectively.

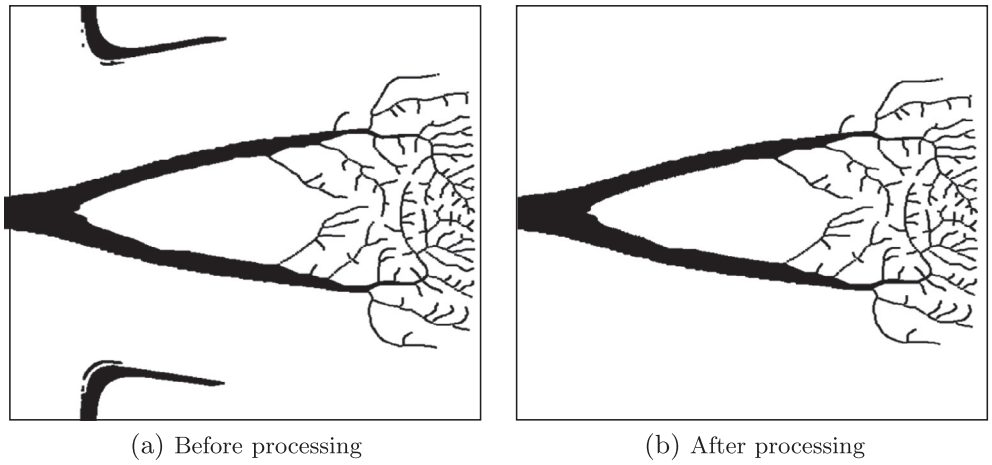

Fig. 12. Optimized design obtained using topology optimization (left), and its post-processed version (right) for the front side of a solar cell under a Gaussian illumination of an average intensity of 12 suns ($A_0 = 20$). The post-processing removed electrode material that remained in dark regions of the cell.

Table 3
Solar cell efficiencies obtained for various illumination and temperature profiles using a reference H-pattern design (denoted by η^*) and topology optimized designs (denoted by η). Here, the term A_0 is used to control the light intensity contrast for the illumination profiles, and T_0 and ΔT_{max} denote the base temperature and amplitude of change in temperature, respectively for the temperature profiles.

Illumination profile	Temperature profile	η^* (in %)	η (in %)	$\Delta\eta = \eta - \eta^*$
Gaussian ($A_0 = 10$)	Uniform ($T_0 = 320$ K)	17.458	17.075	−0.383
Gaussian ($A_0 = 15$)	Uniform ($T_0 = 320$ K)	15.511	17.271	1.760
Gaussian ($A_0 = 20$)	Uniform ($T_0 = 320$ K)	13.366	16.846	3.480
Irregular (multi-Gaussian with $A_0 = 15$ and 20)	Uniform ($T_0 = 320$ K)	16.035	17.463	1.428
Gaussian ($A_0 = 15$)	Gaussian ($T_0 = 320$ K, $\Delta T_{max} = 40$ K)	13.425	15.043	1.618
Gaussian ($A_0 = 15$)	Anti-Gaussian ($T_0 = 320$ K, $\Delta T_{max} = 40$ K)	14.997	16.271	1.274

important for CPVs, and it should therefore be included in the model.

Based on the numerical model, a topology optimization strategy is proposed to design efficient metallization patterns for solar cells under non-uniform illumination and temperature conditions. The applicability of the proposed optimization approach is demonstrated on various synthetic illumination and temperature profiles and for most of the cases, efficient metallization designs are obtained. Using TO, improvement of up to 26% in power output is observed compared to a traditional H-pattern design, optimized for uniform incident sunlight with equivalent average illumination. It is found that a non-uniform temperature distribution can also affect the solar cell performance, and with topology optimization it is possible to design metallization

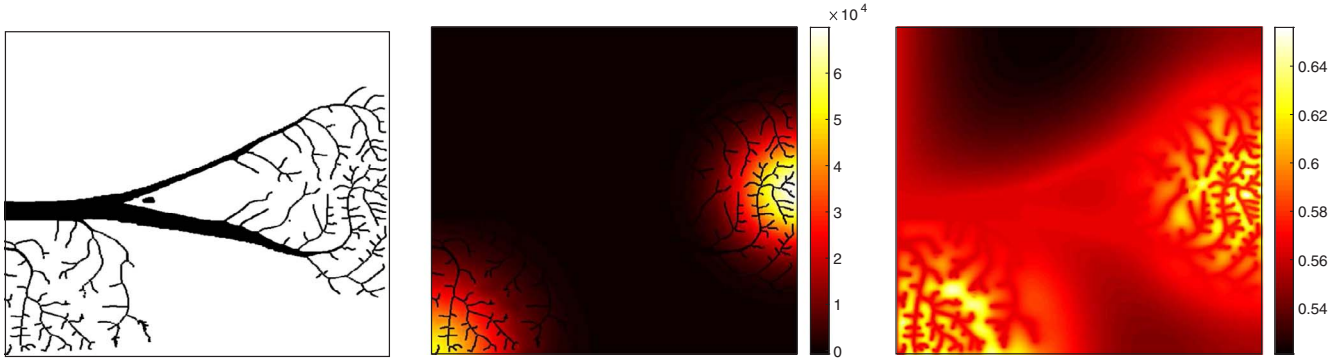

(a) Optimized design (b) Current density (in Am^{-2}) (c) Voltage (in volts)

Fig. 13. Optimized design and the current density and voltage distributions for the front side of a solar cell under an irregular illumination of an average intensity of 12 suns. The irregular profile is obtained using two Gaussian distributions with A_0 values of 15 and 20. A uniform temperature profile is chosen with base temperature set to 320 K. The optimal busbar potential V_b and efficiency η values are 0.563 volts and 17.463%, respectively.

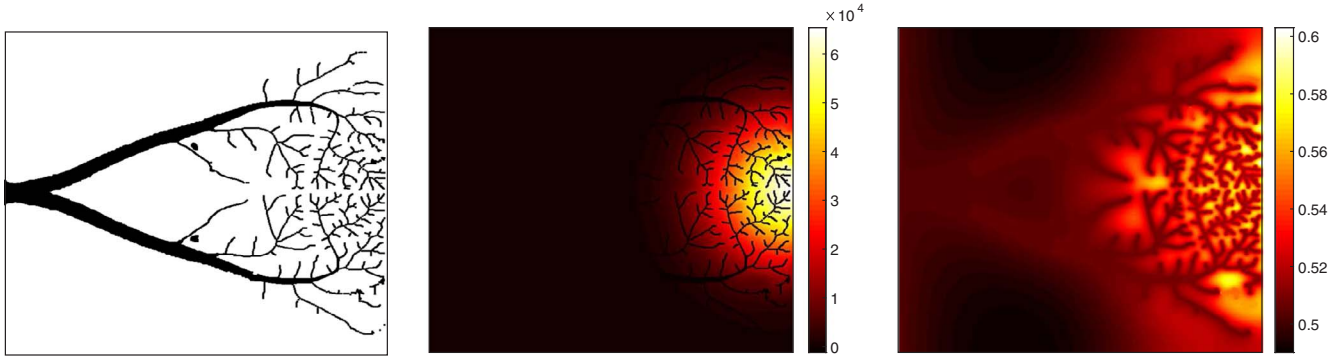

(a) Optimized design (b) Current density (in Am^{-2}) (c) Voltage (in volts)

Fig. 14. Optimized design and the current density and voltage distributions for the front side of a solar cell under a Gaussian illumination of an average intensity of 12 suns ($A_0 = 15$) and a Gaussian temperature profile with base temperature of 320 K and temperature amplitude equal to 40 K. The optimal busbar potential V_b and efficiency η values are 0.503 volts and 15.033%, respectively.

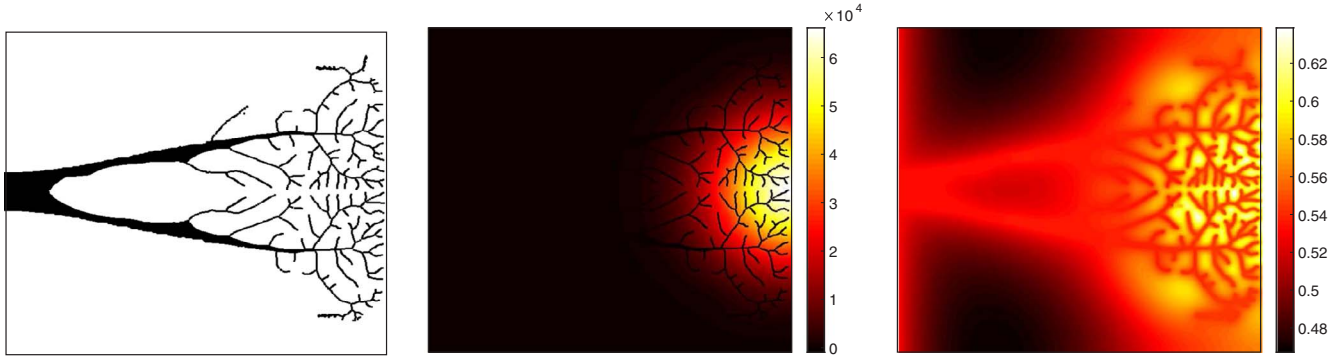

(a) Optimized design (b) Current density (in Am^{-2}) (c) Voltage (in volts)

Fig. 15. Optimized design and the current density and voltage distributions for the front side of a solar cell under a Gaussian illumination of an average intensity of 12 suns ($A_0 = 15$) and an anti-Gaussian temperature profile with base temperature of 320 K and temperature amplitude equal to 40 K. The optimal busbar potential V_b and efficiency η values are 0.532 volts and 16.271%, respectively.

patterns tailored for such profiles. Based on the improvement in performance observed for various cases presented in this study, it can be argued that the proposed approach could serve as an important tool to design solar cell metallizations tailored for concentrated sunlight.

Acknowledgements

This work is part of the Industrial Partnership Programme (IPP) 'Computational sciences for energy research' of the Foundation for Fundamental Research on Matter (FOM), which is part of the Netherlands Organisation for Scientific Research (NWO). This research programme is co-financed by Shell Global Solutions International B.V. We also thank Prof. Arthur Weeber and Dr. René van Swaaij for the helpful discussions, and Prof. Krister Svanberg for providing the MMA subroutine.

Appendix A. Computing $\mathbf{I}^e$

Taking the non-uniform illumination and shading effects into account, I^e for any element can be calculated as

$$I^e = I_L(1-\rho)^r\mathscr{R} - I_{01}\left(e^{\frac{\beta(V^e+I^e\widetilde{R}_s)}{n_1}}-1\right) - I_{02}\left(e^{\frac{\beta(V^e+I^e\widetilde{R}_s)}{n_2}}-1\right) - \frac{V^e + I^e\widetilde{R}_s}{R_{SH}}. \tag{A.1}$$

This is a transcendental equation and cannot be solved directly. Thus, we solve it numerically using inner Newton iterations. Eq. (A.1) is rewritten as

$$I^e - I_L(1-\rho)^r\mathscr{R} + I_{01}\left(e^{\frac{\beta(V+I\widetilde{R}_s)}{n_1}}-1\right) + I_{02}\left(e^{\frac{\beta(V+I\widetilde{R}_s)}{n_2}}-1\right) + \frac{V^e + I^e\widetilde{R}_s}{R_{SH}} = 0. \tag{A.2}$$

Using (A.2) with some rearrangements, a function ψ is defined for any element of the emitter layer as

$$\psi(I^e) = I^e\left(1 + \frac{\widetilde{R}_s}{R_{SH}}\right) + I_{01}e^{\frac{\beta(V^e+I^e\widetilde{R}_s)}{n_1}} + I_{02}e^{\frac{\beta(V+I^e\widetilde{R}_s)}{n_2}} - \left(I_L(1-\rho)^r\mathscr{R} + I_{01} + I_{02} - \frac{V^e}{R_{SH}}\right) = 0. \tag{A.3}$$

To obtain $\mathbf{I}^e$,$\psi(I^e)$ needs to be assembled for all the finite elements of the domain and the root of equation $\boldsymbol{\psi}(\mathbf{I}^e) = \mathbf{0}$ needs to be calculated. This is achieved using Newton method, where following is the update scheme:

$$\mathbf{I}^e_{i+1} = \mathbf{I}^e_i - \frac{\boldsymbol{\psi}(\mathbf{I}^e)}{\boldsymbol{\psi}'(\mathbf{I}^e)}, \tag{A.4}$$

where $\psi'(I^e)$ for any finite element is stated as

$$\psi'(I^e) = \left(1 + \frac{\widetilde{R}_s}{R_{SH}}\right) + \frac{\beta\widetilde{R}_sI_{01}}{n_1}e^{\frac{\beta(V^e+I^e\widetilde{R}_s)}{n_1}} + \frac{\beta\widetilde{R}_sI_{02}}{n_2}e^{\frac{\beta(V^e+I^e\widetilde{R}_s)}{n_2}}. \tag{A.5}$$

Appendix B. Computing $\frac{d\mathbf{I}^e}{d\mathbf{V}^e}$

From Eq. (A.1), it can be seen that the current at any point of the emitter layer depends only on the local voltage. Thus, $\frac{d\mathbf{I}^e}{d\mathbf{V}^e}$ can be obtained by assembling the terms $\frac{dI^e}{dV^e}$ for the whole finite element domain. For $\frac{dI^e}{dV^e}$, the derivative of Eq. (A.2) with respect to V^e is taken and the following is obtained:

$$\frac{dI^e}{dV^e} + \frac{\beta I_{01}}{n_1}\left(1 + \widetilde{R}_s\frac{dI^e}{dV^e}\right)e^{\frac{\beta(V+I^e\widetilde{R}_s)}{n_1}} + \frac{\beta I_{02}}{n_2}\left(1 + \widetilde{R}_s\frac{dI^e}{dV^e}\right)e^{\frac{\beta(V+I^e\widetilde{R}_s)}{n_2}} + \frac{1}{R_{SH}} + \frac{\widetilde{R}_s}{R_{SH}}\frac{dI^e}{dV^e} = 0. \tag{B.1}$$

Rewriting in terms of $\frac{dI^e}{dV^e}$,

$$\frac{dI^e}{dV^e} = -\frac{\frac{\beta I_{01}}{n_1}e^{\beta(V+I^e\widetilde{R}_s)/n_1} + \frac{\beta I_{02}}{n_2}e^{\beta(V+I^e\widetilde{R}_s)/n_2} + \frac{1}{R_{SH}}}{\left(1 + \frac{\beta\widetilde{R}_sI_{01}}{n_1}e^{\beta(V+I^e\widetilde{R}_s)/n_1} + \frac{\beta\widetilde{R}_sI_{02}}{n_2}e^{\beta(V+I^e\widetilde{R}_s)/n_2} + \frac{\widetilde{R}_s}{R_{SH}}\right)} \tag{B.2}$$

Appendix C. IV curves for concentrated illuminations

The IV curve stated in Eq. (6) can be written for 1-diode model ($n_2 = \infty$) and expressed in terms of current density J^e as

$$J^e = J_L - J_{01}\left(e^{\frac{\beta(V+J^e\mathscr{A}\widetilde{R}_s)}{n_1}}-1\right) - \frac{V/\mathscr{A} + J^e\widetilde{R}_s}{R_{SH}}. \tag{C.1}$$

where $\mathscr{A}$ denotes the local area, and J_L and J_{01} refer to photoillumination current density and dark current density in diode 1, respectively. Comparing Eqs. (24) and (C.1), following is obtained:

$$J_L = C_1G, \tag{C.2}$$

$$J_{01} = C_2T^3\left(e^{\frac{-E_g}{k_bT}}\right), \tag{C.3}$$

$$\widetilde{R}_s = 0, \tag{C.4}$$

$$R_{SH} = \frac{1}{\mathscr{A}C_3}. \tag{C.5}$$

Appendix D. Sensitivity analysis

For clarity, we assume $\mathbf{W}_1 = \mathbf{K}^e + \frac{1}{R_c}\mathbb{I}$,$\mathbf{W}_2 = -\frac{1}{R_c}\mathbb{I}$ and $\mathbf{W}_3 = \mathbf{K}^m + \frac{1}{R_c}\mathbb{I}$ and Eq. (28) is rewritten as

$$\widehat{\mathscr{J}} = \mathscr{J} + \boldsymbol{\lambda}_e^{\mathrm{T}}(\mathbf{W}_1\mathbf{V}^e + \mathbf{W}_2\mathbf{V}^m - \mathbf{I}^e) + \begin{bmatrix}\boldsymbol{\lambda}_{mf}\\ \boldsymbol{\lambda}_{mp}\end{bmatrix}^{\mathrm{T}}(\mathbf{W}_2\mathbf{V}^e + \mathbf{W}_3\mathbf{V}^m), \tag{D.1}$$

where, the subscripts *mf* and *mp* refer to the free degreees and fixed degrees of freedom, respectively for the metal electrode layer. Eq. (D.1) should

hold for all values of $\boldsymbol{\lambda}_e$ and $\boldsymbol{\lambda}_m$. Thus, we can reduce it by putting $\boldsymbol{\lambda}_{mp} = \mathbf{0}$. Thus, we obtain

$$\widehat{\mathscr{J}} = \mathscr{J} + \boldsymbol{\lambda}_e^{\intercal}(\mathbf{W}_1\mathbf{V}^e + \mathbf{W}_2\mathbf{V}^m - \mathbf{I}^e) + \boldsymbol{\lambda}_{mf}^{\intercal}([\mathbf{W}_{2ff}\ \ \mathbf{W}_{2fp}]\mathbf{V}^e + [\mathbf{W}_{3ff}\ \ \mathbf{W}_{3fp}]\mathbf{V}^m), \tag{D.2}$$

where $\mathbf{W}_2 = \begin{bmatrix} \mathbf{W}_{2ff} & \mathbf{W}_{2fp} \\ \mathbf{W}_{2pf} & \mathbf{W}_{2pp} \end{bmatrix}$ and $\mathbf{W}_3 = \begin{bmatrix} \mathbf{W}_{3ff} & \mathbf{W}_{3fp} \\ \mathbf{W}_{3pf} & \mathbf{W}_{3pp} \end{bmatrix}$.

Taking the derivative of Eq. (D.2) with respect to the design variables' set $\mathbf{s}$,

$$\begin{aligned} \frac{d\widehat{\mathscr{J}}}{d\mathbf{s}} &= \frac{\partial \mathscr{J}}{\partial \mathbf{s}} + \frac{\partial \mathscr{J}}{\partial \mathbf{V}^e}\frac{d\mathbf{V}^e}{d\mathbf{s}} + \frac{\partial \mathscr{J}}{\partial \mathbf{V}^m}\frac{d\mathbf{V}^m}{d\mathbf{s}} \\ &+ \boldsymbol{\lambda}_e^{\intercal}\left(\frac{d\mathbf{W}_1}{d\mathbf{s}}\mathbf{V}^e + \mathbf{W}_1\frac{d\mathbf{V}^e}{d\mathbf{s}} + \frac{d\mathbf{W}_2}{d\mathbf{s}}\mathbf{V}^m + \mathbf{W}_2\frac{d\mathbf{V}^m}{d\mathbf{s}} - \frac{\partial \mathbf{I}^e}{\partial \mathbf{s}} - \frac{\partial \mathbf{I}^e}{\partial \mathbf{V}^e}\frac{d\mathbf{V}^e}{d\mathbf{s}} - \frac{\partial \mathbf{I}^e}{\partial \mathbf{V}^m}\frac{d\mathbf{V}^m}{d\mathbf{s}}\right) \\ &+ \boldsymbol{\lambda}_{mf}^{\intercal}\left(\left[\frac{d\mathbf{W}_{2ff}}{d\mathbf{s}}\ \ \frac{d\mathbf{W}_{2fp}}{d\mathbf{s}}\right]\mathbf{V}^e + [\mathbf{W}_{2ff}\ \ \mathbf{W}_{2fp}]\frac{d\mathbf{V}^e}{d\mathbf{s}} + \left[\frac{d\mathbf{W}_{3ff}}{d\mathbf{s}}\ \ \frac{d\mathbf{W}_{3fp}}{d\mathbf{s}}\right]\mathbf{V}^m + [\mathbf{W}_{3ff}\ \ \mathbf{W}_{3fp}]\frac{d\mathbf{V}^m}{d\mathbf{s}}\right). \end{aligned} \tag{D.3}$$

Since $\mathbf{W}_1$ and $\mathbf{W}_2$ are constant matrices, the associated derivative terms with respect to $\mathbf{s}$ can be set to $\mathbf{0}$. In addition, since $\mathscr{J}$ and $\mathbf{I}^e$ do not have a direct dependence on $\mathbf{V}^m$, the terms $\frac{\partial \mathscr{J}}{\partial \mathbf{V}^m}$ and $\frac{\partial \mathbf{I}^e}{\partial \mathbf{V}^m}$ can be set to $\mathbf{0}$. Taking these into consideration,

$$\begin{aligned} \frac{d\widehat{\mathscr{J}}}{d\mathbf{s}} &= \frac{\partial \mathscr{J}}{\partial \mathbf{s}} + \frac{\partial \mathscr{J}}{\partial \mathbf{V}^e}\frac{d\mathbf{V}^e}{d\mathbf{s}} + \boldsymbol{\lambda}_e^{\intercal}\left(\mathbf{W}_1\frac{d\mathbf{V}^e}{d\mathbf{s}} + \mathbf{W}_2\frac{d\mathbf{V}^m}{d\mathbf{s}} - \frac{\partial \mathbf{I}^e}{\partial \mathbf{s}} - \frac{\partial \mathbf{I}^e}{\partial \mathbf{V}^e}\frac{d\mathbf{V}^e}{d\mathbf{s}}\right) \\ &+ \boldsymbol{\lambda}_{mf}^{\intercal}\left([\mathbf{W}_{2ff}\ \ \mathbf{W}_{2fp}]\frac{d\mathbf{V}^e}{d\mathbf{s}} + \left[\frac{d\mathbf{W}_{3ff}}{d\mathbf{s}}\ \ \frac{d\mathbf{W}_{3fp}}{d\mathbf{s}}\right]\mathbf{V}^m + [\mathbf{W}_{3ff}\ \ \mathbf{W}_{3fp}]\frac{d\mathbf{V}^m}{d\mathbf{s}}\right). \end{aligned} \tag{D.4}$$

Rearranging the terms and putting $\mathbf{V}^m = \begin{bmatrix} \mathbf{V}_f^m \\ \mathbf{V}_p^m \end{bmatrix}$,

$$\begin{aligned} \frac{d\widehat{\mathscr{J}}}{d\mathbf{s}} &= \frac{\partial \mathscr{J}}{\partial \mathbf{s}} + \boldsymbol{\lambda}_e^{\intercal}\begin{bmatrix} \mathbf{W}_{2fp} \\ \mathbf{W}_{2pp} \end{bmatrix}\frac{d\mathbf{V}_p^m}{d\mathbf{s}} - \boldsymbol{\lambda}_e^{\intercal}\frac{\partial \mathbf{I}^e}{\partial \mathbf{s}} + \boldsymbol{\lambda}_{mf}^{\intercal}\left[\frac{d\mathbf{W}_{3ff}}{d\mathbf{s}}\ \ \frac{d\mathbf{W}_{3fp}}{d\mathbf{s}}\right]\mathbf{V}^m + \boldsymbol{\lambda}_{mf}^{\intercal}\mathbf{W}_{3fp}\frac{d\mathbf{V}_p^m}{d\mathbf{s}} \\ &+ \left(\frac{\partial \mathscr{J}}{\partial \mathbf{V}^e} + \boldsymbol{\lambda}_e^{\intercal}\mathbf{W}_1 - \boldsymbol{\lambda}_e^{\intercal}\frac{\partial \mathbf{I}^e}{\partial \mathbf{V}^e} + \boldsymbol{\lambda}_{mf}^{\intercal}[\mathbf{W}_{2ff}\ \ \mathbf{W}_{2fp}]\right)\frac{d\mathbf{V}^e}{d\mathbf{s}} \\ &+ \left(\boldsymbol{\lambda}_e^{\intercal}\begin{bmatrix} \mathbf{W}_{2ff} \\ \mathbf{W}_{2pf} \end{bmatrix} + \boldsymbol{\lambda}_{mf}^{\intercal}\mathbf{W}_{3ff}\right)\frac{d\mathbf{V}_f^m}{d\mathbf{s}}. \end{aligned} \tag{D.5}$$

To eliminate $\frac{d\mathbf{V}^e}{d\mathbf{s}}$ and $\frac{d\mathbf{V}_f^m}{d\mathbf{s}}$, we define the following adjoint problem:

$$\frac{\partial \mathscr{J}}{\partial \mathbf{V}^e} + \boldsymbol{\lambda}_e^{\intercal}\mathbf{W}_1 - \boldsymbol{\lambda}_e^{\intercal}\frac{\partial \mathbf{I}^e}{\partial \mathbf{V}^e} + \boldsymbol{\lambda}_{mf}^{\intercal}[\mathbf{W}_{2ff}\ \ \mathbf{W}_{2fp}] = \mathbf{0}, \tag{D.6}$$

$$\boldsymbol{\lambda}_e^{\intercal}\begin{bmatrix} \mathbf{W}_{2ff} \\ \mathbf{W}_{2pf} \end{bmatrix} + \boldsymbol{\lambda}_{mf}^{\intercal}\mathbf{W}_{3ff} = \mathbf{0}, \tag{D.7}$$

which yields

$$\boldsymbol{\lambda}_e^{\intercal} = -\left(\frac{\partial \mathscr{J}}{\partial \mathbf{V}^e}\right)\left(\mathbf{W}_1 - \frac{\partial \mathbf{I}^e}{\partial \mathbf{V}^e} - \begin{bmatrix} \mathbf{W}_{2ff} \\ \mathbf{W}_{2pf} \end{bmatrix}\mathbf{W}_{3ff}^{-1}[\mathbf{W}_{2ff}\ \ \mathbf{W}_{2fp}]\right)^{-1}, \tag{D.8}$$

$$\boldsymbol{\lambda}_{mf}^{\intercal} = \left(\frac{\partial \mathscr{J}}{\partial \mathbf{V}^e}\right)\left(\mathbf{W}_1 - \frac{\partial \mathbf{I}^e}{\partial \mathbf{V}^e} - \begin{bmatrix} \mathbf{W}_{2ff} \\ \mathbf{W}_{2pf} \end{bmatrix}\mathbf{W}_{3ff}^{-1}[\mathbf{W}_{2ff}\ \ \mathbf{W}_{2fp}]\right)^{-1}\begin{bmatrix} \mathbf{W}_{2ff} \\ \mathbf{W}_{2pf} \end{bmatrix}\mathbf{W}_{3ff}^{-1}. \tag{D.9}$$

Using the values of $\boldsymbol{\lambda}_e$ and $\boldsymbol{\lambda}_{mf}$ given in Eqs. (D.8) and (D.9), Eq. (D.5) simplifies to

$$\frac{d\widehat{\mathscr{J}}}{d\mathbf{s}} = \frac{\partial \mathscr{J}}{\partial \mathbf{s}} + \boldsymbol{\lambda}_e^{\intercal}\begin{bmatrix} \mathbf{W}_{2fp} \\ \mathbf{W}_{2pp} \end{bmatrix}\frac{d\mathbf{V}_p^m}{d\mathbf{s}} - \boldsymbol{\lambda}_e^{\intercal}\frac{\partial \mathbf{I}^e}{\partial \mathbf{s}} + \boldsymbol{\lambda}_{mf}^{\intercal}\left[\frac{d\mathbf{W}_{3ff}}{d\mathbf{s}}\ \ \frac{d\mathbf{W}_{3fp}}{d\mathbf{s}}\right]\mathbf{V}^m + \boldsymbol{\lambda}_{mf}^{\intercal}\mathbf{W}_{3fp}\frac{d\mathbf{V}_p^m}{d\mathbf{s}}. \tag{D.10}$$

D.1. Computing $\frac{d\widetilde{\mathscr{J}}}{d\rho}$

To calculate the sensitivities of the augmented response $\widetilde{\mathscr{J}}$ with respect to the design density field $\boldsymbol{\rho}$,$\mathbf{s}$ is replaced by $\boldsymbol{\rho}$ in Eq. (D.10). Since $\mathbf{V}_p^m$ does not depend on material distribution, $\frac{d\mathbf{V}_p^m}{d\rho} = \mathbf{0}$. Thus,

$$\frac{d\widehat{\mathscr{J}}}{d\rho} = \frac{\partial \mathscr{J}}{\partial \rho} - \boldsymbol{\lambda}_e^{\intercal}\frac{\partial \mathbf{I}^e}{\partial \rho} + \boldsymbol{\lambda}_{mf}^{\intercal}\left[\frac{d\mathbf{W}_{3ff}}{d\rho}\ \ \frac{d\mathbf{W}_{3fp}}{d\mathbf{s}}\right]\mathbf{V}^m. \tag{D.11}$$

From Eq. (26), $\frac{\partial \mathscr{J}}{\partial \rho} = \frac{\partial}{\partial \rho}(V_b\sum_{i=1}^{N_{el}} I_i^e) = \frac{\partial}{\partial \rho}(V_b\mathbf{1}^{\intercal}\mathbf{I}^e) = V_b\mathbf{1}^{\intercal}\left(\frac{\partial \mathbf{I}^e}{\partial \rho}\right)$, where $\frac{\partial \mathbf{I}^e}{\partial \rho}$ can be calculated as discussed in Appendix E.

D.2. Computing $\frac{d\widetilde{\mathscr{J}}}{dV_b}$

To calculate the sensitivities of the augmented response $\widetilde{\mathscr{J}}$ with respect to the busbar potential V_b,$\mathbf{s}$ is replaced by V_b in Eq. (D.10). Also, $\mathbf{W}_3$ and $\mathbf{I}^e$ do not depend on V_b and $\frac{d\mathbf{V}_p^m}{dV_b} = \mathbf{1}$. Thus,

$$\frac{d\hat{\mathscr{I}}}{dV_b} = \frac{\partial \mathscr{I}}{\partial V_b} + \boldsymbol{\lambda}_e^{\mathsf{T}} \begin{bmatrix} \mathbf{W}_{2fp} \\ \mathbf{W}_{2pp} \end{bmatrix} \mathbf{1} + \boldsymbol{\lambda}_{mf}^{\mathsf{T}} \mathbf{W}_{3fp} \mathbf{1}. \tag{D.12}$$

From Eq. (26), $\frac{\partial \mathscr{I}}{\partial V_b} = \frac{\partial}{\partial V_b}\left(V_b \sum_{i=1}^{N_{el}} I_i^e\right) = \sum_{i=1}^{N_{el}} I_i^e$.

Appendix E. Computing $\frac{\partial \mathbf{I}^e}{\partial \rho}$

The photoillumination current at any point on the emitter surface is assumed to depend on the shading only at that point. Thus, $\frac{\partial \mathbf{I}^e}{\partial \rho}$ can be obtained by assembling the terms $\frac{\partial I^e}{\partial \rho}$ for the whole finite element domain. Thus, Taking the derivative of Eq. (A.2) w.r.t ρ, following is obtained:

$$\frac{\partial I^e}{\partial \rho} + I_L r (1-\rho)^{r-1} \mathscr{R} + \frac{I_{01}\beta \widetilde{R}_s}{n_1} \frac{\partial I^e}{\partial \rho} e^{\beta (V^e + I^e \widetilde{R}_s)/n_1} + \frac{I_{02}\beta \widetilde{R}_s}{n_2} \frac{\partial I^e}{\partial \rho} e^{\beta (V^e + I^e \widetilde{R}_s)/n_2} + \frac{\widetilde{R}_s}{R_{SH}} \frac{\partial I^e}{\partial \rho} = 0. \tag{E.1}$$

Putting together all the terms with $\frac{dJ}{dV}$,

$$\frac{\partial I^e}{\partial \rho}\left(1 + \frac{I_{01}\beta \widetilde{R}_s}{n_1} e^{\beta (V^e + I^e \widetilde{R}_s)/n_1} + \frac{I_{02}\beta \widetilde{R}_s}{n_2} e^{\beta (V^e + I^e \widetilde{R}_s)/n_2} + \frac{\widetilde{R}_s}{R_{SH}}\right) = -I_L r (1-\rho)^{r-1} \mathscr{R}. \tag{E.2}$$

This further simplifies to

$$\frac{\partial I^e}{\partial \rho} = \frac{-I_L r (1-\rho)^{r-1} \mathscr{R}}{1 + \frac{I_{01}\beta \widetilde{R}_s}{n_1} e^{\beta (V^e + I^e \widetilde{R}_s)/n_1} + \frac{I_{02}\beta \widetilde{R}_s}{n_2} e^{\beta (V^e + I^e \widetilde{R}_s)/n_2} + \frac{\widetilde{R}_s}{R_{SH}}}. \tag{E.3}$$

References

Algora, C., Díaz, V., 2000. Influence of series resistance on guide-lines for manufacture of concentrator p-on-n GaAs solar cells. Prog. Photovoltaics Res. Appl. 8, 211–225.

Baig, H., Heasman, K.C., Mallick, T.K., 2012. Non-uniform illumination in concentrating solar cells. Renew. Sustain. Energy Rev. 12, 5890–5909.

Beckman, W.A., 1967. Optimization of contact grid spacing for high solar flux photovoltaic cells. J. Eng. Power 89 (3), 415–418.

Bendsøe, M.P., 1989. Optimal shape design as a material distribution problem. Structural Optimization 1 (4), 193–202.

Bendsøe, M.P., Sigmund, O., 2003. Topology Optimization: Theory, methods and applications. Springer.

Bissels, G.M.M.W., Asselbergs, M.A.H., Schermer, J.J., Haverkemp, E.J., Smeenk, N.J., Vlieg, E., 2011. A genuine circular contact grid pattern for solar cells. Prog. Photovoltaics Res. Appl. 18, 517–526.

Bruns, T.E., Tortorelli, D.A., 2001. Topology optimization of nonlinear structures and compliant mechanisms. Comput. Methods Appl. Mech. Eng. 190, 3443–3459.

Burgers, A.R., 1999. How to design optimal metallization patterns for solar cells. Prog. Photovoltaics Res. Appl. 7 (6), 457–461.

Burgers, A., 2005. New Metallization Patterns and Analysis of Light Trapping for Silicon Solar Cells. PhD Thesis. .

Conti, M., 1981. Optimal design of front-contact metallization for photovoltaic solar cells. Solid-State Electron. 24 (1), 79–83.

Domenech-Garret, J.L., 2011. Cell behaviour under different non-uniform temperature and radiation combined profiles using a two dimensional finite element model. Sol. Energy 85, 256–264.

Flat, A., Milnes, A.G., 1979. Optimization of multi-layer front-contact grid patterns for solar cells. Sol. Energy 23, 289–299.

Franklin, E., Coventry, J.S., 2003. Effects of highly non-uniform illumination distribution on electrical performance of solar cells. In: Proceedings of Solar. Australian and New Zealand Solar Society.

Galiana, B., Algora, C., Rey-Stolle, I., Vara, I.G., 2005. A 3-D model for concentrator solar cells based on distributed circuit units. IEEE Trans. Electron Dev. 52 (12), 2552–2558.

Guest, J., Prevost, J., Belytschko, T., 2004. Achieving minimum length scale in topology optimization using nodal design variables and projection functions. Int. J. Numer. Meth. Eng. 61 (2), 238–254.

Gupta, D.K., Langelaar, M., Barink, M., van Keulen, F., 2014. Topology optimization: an effective method for designing front metallization patterns of solar cells. In: IEEE 40th Photovoltaic Specialists Conference. IEEE, pp. 1–6.

Gupta, D.K., Langelaar, M., Barink, M., van Keulen, F., 2015. Topology optimization of front metallization patterns for solar cells. Struct. Multidiscipl. Optimiz. 51, 941–955.

Gupta, D.K., Langelaar, M., Barink, M., van Keulen, F., 2016. Optimizing front metallization patterns: efficiency with aesthetics in free-form solar cells. Renew. Energy 86, 1332–1339.

Gupta, D.K., Barink, M., Galagan, Y., Langelaar, M., 2017. Integrated front-rear-grid optimization in free-form solar cells. IEEE J. Photovoltaics 7 (1), 294–302.

Johnston, G., 1998. Focal region measurements of the 20 m^2 tiled dish at the Australian National University. Sol. Energy 63, 117–124.

Luque, A., Sala, G., Arboiro, J., 1998. Electric and thermal model for non-uniformly illuminated concentration cells. Sol. Energy Mater. Sol. Cells 51, 269–290.

Meier, D.L., Schroder, D.K., 1984. Contact resistance: its measurement and relative importance to power loss in a solar cell. IEEE Trans. Electron Dev. 31 (5), 647–653.

Mellor, A., Domenech-Garret, J., Chemisana, D., Rosell, I., 2009. A two-dimensional finite element model of front surface current flow in cells under non-uniform, concentrated illumination. Sol. Energy 83, 1459–1465.

Mitchell, K.W., 1977. Computer analysis of resistance and non-uniform illumination effects on concentrator solar cells. In: International Electron Devices Meeting, pp. 229–232.

Moore, A.R., 1979. An optimized grid design for a sun-concentrator solar cell. RCA Rev. 40, 140–152.

Rosell, J.I., Ibañez, M., 2006. Modelling power output in photovoltaic modules for outdoor operating conditions. Energy Convers. Manage. 47, 2424–2430.

Schroder, D., Meier, D.L., 1984. Solar cell contact resistance – a review. IEEE Trans. Electron Dev. 31, 637–647.

Shockley, W., 1950. In: Electrons and Holes in Semiconductors: With Applications to Transistor Electronics.

Sigmund, O., 2007. Morphology-based black and white filters for topology optimization. Struct. Multidiscipl. Optimiz. 33, 401–424.

Svanberg, K., 1987. The method of moving asymptotes – a new method for structural optimization. Int. J. Numer. Meth. Eng. 24, 359–373.

van Deelen, J., Tezsevin, Y., Barink, M., 2016. Multi-material front contact for 19% thin film solar cells. Materials 9 (2), 96.

van Keulen, F., Haftka, R.T., Kim, N.H., 2005. Review of options for structural design sensitivity analysis. Part 1: Linear systems. Comput. Methods Appl. Mech. Eng. 194, 3213–3243.

Wolf, M., Rauschenbach, H., 1963. Series resistance effects on solar cell measurements. Adv. Energy Convers. 3 (2), 455–479.

Wong, J., Mueller, T., Sridharan, R., Zhang, X., Yang, Y., Feng, Z., Huang, Q., Verlinden, P., Aberle, A.G., 2011. Series resistance modeling of complex metallization geometries of solar cells using conductive line decomposition. In: IEEE 38th Photovoltaic Specialists Conference. IEEE, pp. 501–504.

Zienkiewicz, O.C., Taylor, R.L., Zhu, J.Z., 2005. Finite Element Method: Its Basis and Fundamentals. Elsevier.